metals

MDPI

Article

How Austenitic Is a Martensitic Steel Produced by Laser Powder Bed Fusion? A Cautionary Tale

Fan Zhang [1,*], Mark R. Stoudt [1,*], Souzan Hammadi [1,2], Carelyn E. Campbell [1], Eric A. Lass [1,3] and Maureen E. Williams [1]

[1] Material Measurement Laboratory, National Institute of Standards and Technology, Gaithersburg, MD 20899, USA; souzan.hammadi@kemi.uu.se (S.H.); carelyn.campbell@nist.gov (C.E.C.); elass@utk.edu (E.A.L.); maureen.williams@nist.gov (M.E.W.)
[2] Department of Material Science and Engineering, Royal Institute of Technology (KTH), Brinellvägen 23, 100 44 Stockholm, Sweden
[3] Department of Materials Science and Engineering, The University of Tennessee, Knoxville, TN 37996, USA
* Correspondence: fan.zhang@nist.gov (F.Z.); mark.stoudt@nist.gov (M.R.S.); Tel.: +1-301-975-5734 (F.Z.)

Abstract: Accurate phase fraction analysis is an essential element of the microstructural characterization of alloys and often serves as a basis to quantify effects such as heat treatment or mechanical deformation. Additive manufacturing (AM) of metals, due to the intrinsic nonequilibrium solidification and spatial variability, creates additional challenges for the proper quantification of phase fraction. Such challenges are exacerbated when the alloy itself is prone to deformation-induced phase transformation. Using commonly available in-house X-ray diffraction (XRD) and electron backscatter diffraction (EBSD) and less commonly used synchrotron-based high-energy X-ray diffraction, we characterized nitrogen-atomized 17-4 precipitation-hardening martensitic stainless steel, a class of AM alloy that has received broad attention within the AM research community. On the same build, our measurements recovered the entire range of reported values on the austenite phase fractions of as-built AM 17-4 in literature, from ≈100% martensite to ≈100% austenite. Aided by Calphad simulation, our experimental findings established that our as-built AM 17-4 is almost fully austenitic and that in-house XRD and EBSD measurements are subject to significant uncertainties created by the specimen's surface finish. Hence, measurements made using these techniques must be understood in their correct context. Our results carry significant implications, not only to AM 17-4 but also to AM alloys that are susceptible to deformation-induced structure transformation and suggest that characterizations with less accessible but bulk sensitive techniques such as synchrotron-based high energy X-ray diffraction or neutron diffraction may be required for proper understanding of these materials.

Keywords: additive manufacturing; 17-4 steel; phase fraction; X-ray diffraction; electron backscatter diffraction; CALPHAD; laser-powder bed fusion

Citation: Zhang, F.; Stoudt, M.R.; Hammadi, S.; Campbell, C.E.; Lass, E.A.; Williams, M.E. How Austenitic Is a Martensitic Steel Produced by Laser Powder Bed Fusion? A Cautionary Tale. *Metals* **2021**, *11*, 1924. https://doi.org/10.3390/met11121924

Academic Editor: João Pedro Oliveira

Received: 1 October 2021
Accepted: 22 November 2021
Published: 29 November 2021

1. Introduction

Additive manufacturing (AM) of metals represents a suite of emerging manufacturing technologies that allow fabrication of parts with complex shapes and geometries in a single manufacturing step [1]. AM is an extension of the digital transformation in the manufacturing domain and leads to many exciting innovations that promise to deliver new and cost-effective products to their customers, both faster and with better performance. Compared with conventional metallurgical manufacturing approaches, which are usually based on equilibrium or near-equilibrium solidification, AM relies on nonequilibrium solidification [2]. This characteristic of AM processing, in turn, is often regarded as the dominant factor that determines the microstructure of AM parts. Our limited understanding of the processing (solidification)–structure–property relationship presents a major hurdle to the

qualification and certification of high-value added AM parts for various industrial sectors, such as defense and aerospace [3,4].

A fundamental element of the microstructural characterization of alloys is their phase composition and distribution. This is essential to many aspects of metallurgical science, including development of new alloys, optimization of alloy fabrication technologies, and design and control of heat treatment protocols, aimed at the desired mechanical, physical, and chemical properties. Accurate assessment of the phases also influences alloy performance predictability in applications [5]. Previous studies have clearly demonstrated that, for many types of AM alloys, even when the starting feedstock materials have the correct composition and phases, due to the rapid solidification ubiquitous to AM, the as-built part can have either unexpected phases [6–9] or unexpected elemental distribution that can lead to unforeseen solid-state transformation during post processing [10–14]. Because of these reasons, we must understand the effect of nonequilibrium solidification on the phase landscape of AM parts in their as-built states, which, in turn, forms a basis of the numerical models that pursue optimization strategies for fabrication and post-processing, a crucial component for the advancement of AM technologies due to their vast parameter space.

X-ray or electron-based diffraction methods are the most common phase characterization techniques due to their wide availability. Data acquired using these techniques are routinely part of published research of AM alloys. For some AM alloys, particularly those that are subject to deformation-induced phase transformations or those whose processing conditions lead to large compositional variations, the variability of the reported values can be confusing. In this work, we will present an in-depth phase-fraction analysis using commonly available characterization techniques such as in-house XRD and EBSD to evaluate their impact on the measured values and discuss the degree of uncertainty of the results.

We use 17-4 martensitic precipitation-hardening (PH) stainless steel (SS) as an example to demonstrate and explain the variation in measured phase fractions. Most steels are highly weldable, which makes them prime candidates for AM processing. In fact, steel represents the most widely used class of AM alloys. Stainless steels, due to their many benefits, such as corrosion, fire, heat, and impact resistance, and long-term value, occupy nearly half of the AM steel market share [15]. The 17-4 PH SS has one of the highest tensile strengths of SS and, due to its high chromium content, attractiveness for applications requiring high strength, high hardness, and good corrosion resistance. Because of these reasons, 17-4 PH is perhaps the most studied precipitation-hardening stainless steels by the AM research community so far. Notably, while 17-4 PH is designed as a martensitic steel and wrought 17-4 PH is almost 100% martensitic, a large variation in the reported phase fractions of as-built materials exists in literature. To gain insight and address this variation, we performed a controlled and systematic investigation using different analytical techniques and interrogated the consistency of the orthogonally acquired experimental values. We will also present a thermodynamic modeling effort to substantiate our experimental findings.

2. Materials and Methods

2.1. Materials

We acquired N_2-atomized 17-4 powders (Stainless Steel GP1) from EOS (Electro-Optical Systems. (Certain commercial equipment, instruments, software, or materials are identified in this paper to foster understanding. Such identification does not imply recommendation or endorsement by the Department of Commerce or the National Institute of Standards and Technology, nor does it imply that the materials or equipment identified are necessarily the best available for the purpose.) Cubes of approximate dimensions of 15 mm × 15 mm × 15 mm were fabricated on an EOS M270 laser powder-bed fusion system. We used an Nd:YAG laser source with an estimated spot size of 50 μm. The source approximately follows a Gaussian shape power distribution. The laser power was set at 195 W. The scanning speed was 800 mm/s and the hatch distance was 100 μm. Using these standard processing parameters recommended by EOS, we built each layer with an approximate layer height at 20 μm. The height of each layer was approximately 20 μm. N_2

with an approximate oxygen level of 0.5% was used as shielding gas during the build. The cube was removed from the substrate using wire-cut electrical discharge machining without a stress-relief heat treatment. The composition of the as-built 17-4 cube was determined using standard chemical analysis, following standards specified by ISO/IEC 17025:2005. These values are reported in Table 1.

Table 1. Measured composition of 17-4 powders used in this work and the allowable range of composition in mass fraction.

Element	Additive 17-4 (Mass Fraction in Percentage)	Standard Range (Mass Fraction in Percentage)
Fe	Balance	Balance
Cr	15.72	15.00–17.50
Ni	4.81	3.00–5.00
Cu	3.74	3.00–5.00
Nb	0.27	0.15–0.45
Mn	0.67	1.00 max
Mo	0.11	-
Si	0.80	1.00 max
C	0.03	0.07 max
S	0.01	0.030 max
P	0.02	0.040 max
N	0.12	-

2.2. Electron Backscatter Diffraction Measurements

We performed electron backscatter diffraction (EBSD) measurements on the as-built AM 17-4 part to identify and determine the distribution of available phases and their fractions. We used an EOL S-7100F (JEOL, Ltd., Akishima, Tokyo, Japan) field emission scanning electron microscopy (SEM) equipped with Oxford NordlysMax2 EBSD detectors, allowing microstructural aspects such as grain morphology, texture, and crystallographic mapping to be explored. We operated the SEM at an accelerating voltage of 20 kV and a beam current of $\approx$ 10 nA to minimize the acquisition time and enhance the EBSD resolution. The EBSD data were acquired with a step size of 0.1 µm and 2 $\times$ 2 binning.

To examine the effect of surface finish on EBSD results, we performed measurements on two surfaces. The first surface was prepared by mechanical polishing to 1 µm roughness, followed by a 16 h vibratory polishing with non-colloidal silica of nominal size of 50 nm. The second surface was prepared following the same protocol as the first surface, after which the surface was subject to a two-step ion milling procedure: (1) 30 min at 400 V, 7 mA and (2) 40 min at 200 V, 2 mA. The goal of the ion milling steps is to remove near-surface materials to reveal the buried sample underlayer.

2.3. In-House X-ray Diffraction Measurement with a Cu Source

We performed a comprehensive study to evaluate the effect of surface finish on the X-ray diffraction (XRD) analysis of phase fraction. We conducted in-house XRD measurements using a Bruker D8 Advance diffractometer (Bruker AXS, Inc., Billerica, MA, USA) equipped with an EIGER2 R 500K (Dectris, Inc., Baden, Switzerland) single-photon-counting detector (we will refer to this type of XRD measurements as in-house measurements hereinafter). The monochromatic X-ray wavelength was 1.5418 Å from the Cu Kα radiation. The XRD scans were focused on a 2 θ range from 10° to 100°, which covers the main diffraction peaks of the martensite and austenite, two phases known to exist in as-built AM 17-4. XRD data were acquired in the Bragg–Brentano (reflection) geometry. Data reduction was conducted using Bruker DIFFRAC.EVA version 5.0 software

and XRD analyses were performed using the Irena package [16] developed on Igor Pro and GSAS-II [17].

We evaluated three surface finishes on the same as-built 17-4 part to cover a spectrum of sample conditions commonly used in XRD characterization of AM 17-4. The first was the as-cut surface. We cut the 17-4 cube using a TechCut Precision Sectioning Machine equipped with an Al_2O_3 blade, operating at 3000 RPM. Measurements were made directly on the as-cut surface. The second surface finish was achieved by sanding the as-cut surface with 800 grit sandpaper until scratches, streaks, or other imperfections were not visibly observed. The third surface was achieved by removing 200 µm material from the 2nd surface, sanding with 800 and 2000 grit sandpapers, followed by a 16 h vibratory polishing with non-colloidal silica (referred to as finely polished hereinafter).

2.4. High-Energy X-ray Diffraction Measurements with a Synchrotron Source

In order to evaluate the bulk phase fraction of the as-built 17-4 alloy, we performed high-energy X-ray diffraction (HEXRD) measurements at 11-ID-B of the Advanced Photon Source, Argonne National Laboratory [18]. The synchrotron HEXRD measurements, unlike in-house XRD measurements above, were conducted in the transmission mode. The X-ray wavelength is 0.2113 Å, which corresponds to an X-ray energy of 58.68 keV. The X-ray flux density is on the order of 10^{13} photon·mm^{-2}·s^{-1}. X-ray beam size was 300 µm × 300 µm. The standard Perkins-Almer 2D area detector was at the beamline and the sample to detector distance was 750 mm; this setup allows a continuous q range from 0.25 Å^{-1} to 7.75 Å^{-1}, where $q = 2\pi/\lambda \times \sin(\theta)$, with θ being one half of the diffraction angle 2 θ and λ being the X-ray wavelength. The instrument was calibrated with the NIST ceria dioxide standard reference material (674b) for X-ray diffraction [19]. A total of 10 XRD measurements were acquired with an acquisition time of 1 s each. The reported data are the sum of 10 XRD measurements.

The HEXRD specimen was cut from the same piece of as-built 17-4 used for in-house XRD measurements. The specimen was ≈1 mm in thickness. The surfaces of this HEXRD specimen were polished on both sides using 800 grit sandpaper.

2.5. Calphad Modeling

To evaluate the micro-segregation during solidification, we performed Calphad modeling using commercial software Thermo-Calc and DICTRA [20]. The solidification behavior was modelled using equilibrium solidification, the Scheil–Gilliver model [21], and DICTRA at different cooling rates. In the DICTRA simulations, local equilibrium was assumed at the interface between different phases and flux balance was maintained for each element. We excluded the effects of dendritic tip diffusion, and the conducted simulations are one dimensional. We used commercial thermodynamic database TCFE7 for these calculations [22] and assumed one half of the interdendritic distance at 200 nm. To increase computational speed, we used a reduced composition for these simulations, where Mn, Si, Nb, Mo, C, P, and S are neglected.

3. Results and Discussions

Phase and phase fraction analysis is a critical component of metal research and essential to the construction of the structure–property relationship. For AM alloys where post-build treatment is often required to eliminate undesired microstructural features such as unwanted phases [23], elemental micro-segregations [10], and microstructural anisotropy [24], or to take advantage of the alloy design and enhance the alloy performance [25], an accurate understanding of the as-built phase landscape serves as the starting point for the design of such post-build treatments. The reported values for many alloys, however, show significant variations. An example for 17-4 PH SS, which is extracted from an incomplete set of existing data [7,26–33], is shown in Figure 1.

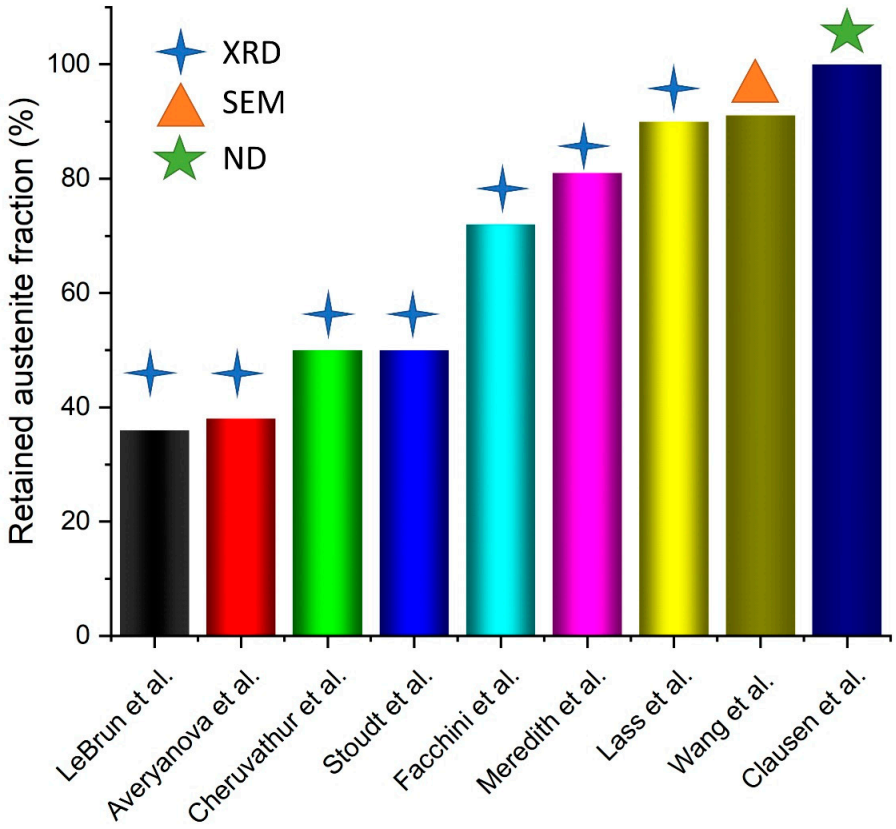

Figure 1. An incomplete set of phase fraction of retained austenite in as-built 17-4 steel, identified in literature. The measurement technique is specified by the symbols on the top of the individual columns. XRD stands for XRD results acquired using in-house X-ray diffractometer. SEM results are acquired from EBSD. ND stands for neutron diffraction.

Figure 1 shows a wide range of the reported retained austenite fraction of as-built 17-4 PH, from ≈35% to nearly 100%. Most of the reported values were acquired using in-house XRD instruments with Cu or Mo X-ray sources. Other techniques that were used to acquire these values include SEM (EBSD) and neutron diffraction (ND). While it is tempting to attribute this level of variation to the complexity intrinsic to metal additive manufacturing, it is worth noting that a number of these studies [28–33] used the same grade powders (GP1) from the same powder vendor (EOS) and the AM parts were fabricated on EOS laser-powder bed fusion systems using their specified GP1 parameter sets. While geometrical shape may affect local cooling rates and batch differences of the starting powders cannot be ruled out, a variation of phase fraction to this extent is unexpected and can make eventual part qualification and certification challenging. It poses an important question, is there anything deeper to these reported values?

To answer this question, we designed a study that builds around the *same* AM 17-4 part and systematically investigated its phase composition and fraction. For the XRD measurements, we sought to capture the position-dependent phase fractions and lattice constants. The schematic of the measurement setup is shown in Figure 2. We chose a 5×5 grid on the surface of the specimen. The mesh spacing along both directions is 3 mm. With a collimated beam size of 1 mm, this reduces the possible overlap of the probed sample volumes between measurements of two neighboring positions. The diffraction pattern was captured on a 2D area detector. The single-photon-counting nature of the detector, when coupled with long counting time, provides the low noise required for quantitative comparison.

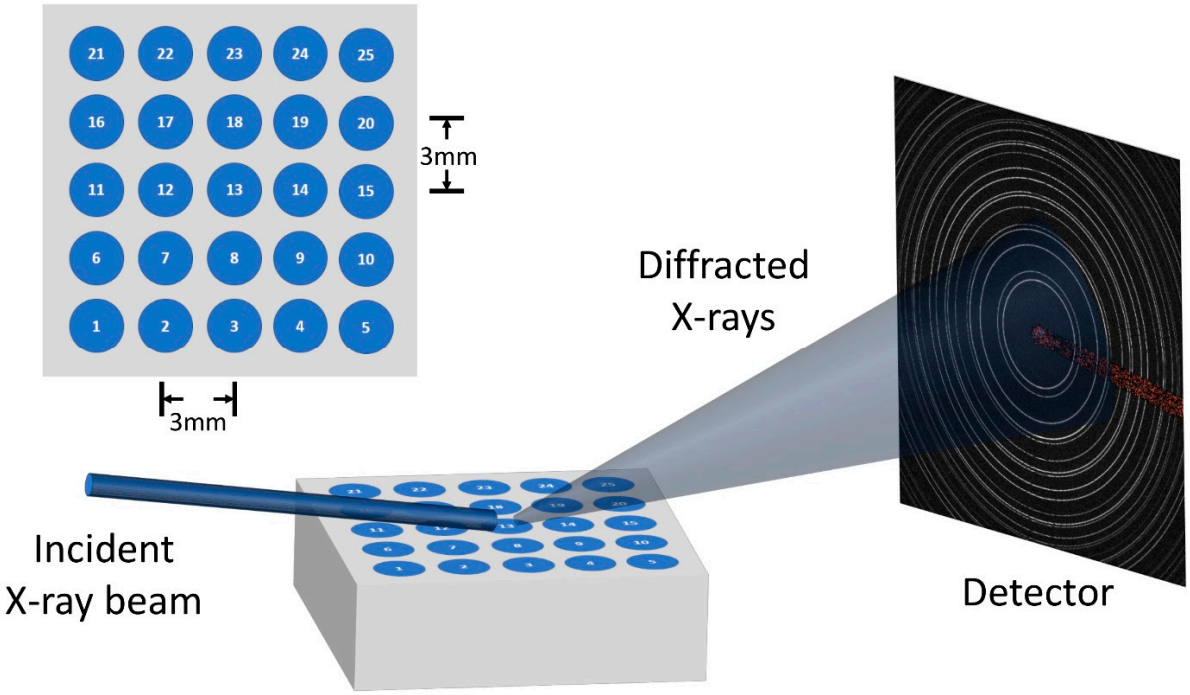

Figure 2. Schematic of the in-house X-ray measurements performed in this study. XRD measurements were conducted with a Bragg–Brentano geometry. A collimated beam with 1 mm beam size was used. XRD data were acquired using an area detector. XRD patterns were acquired at 25 sample positions located on a 5 × 5 grid, as highlighted by the map above.

Figure 3 shows a waterfall plot of 25 sets of in-house XRD data of the as-built 17-4 sample with a finely polished surface. For clarity, only data over a q range between 2.7 Å^{-1} and 3.4 Å^{-1} are shown. XRD data in this q range include the two most intense peaks from austenite and martensite phases, namely, face-centered cubic (FCC, austenite) {111} peak and body-centered cubic (BCC, martensite) {110} peak, as highlighted by the inset. It is worth noting that while martensite is expected to have a body-centered tetragonal structure, the tetragonality is known to be very close to one for this class of AM martensitic steels [31,34], making it impossible to distinguish between BCC and BCT.

The XRD datasets over the entire measured q range can be described by a combination of BCC and FCC lattices. Hence, two conclusions can be drawn immediately. The first is that the as-built AM 17-4 appears to consist *only* of martensite and austenite phases, consistent with most of the existing results shown in Figure 1. The second is that the phase fraction of austenite or martensite appears to be location-dependent and significant variation exists, judging by the 25 sets of XRD data alone.

To evaluate the position dependence of the lattice constants and phase fractions of the austenite and martensite phases, we performed a quantitative analysis and calculated the diffraction intensity of a given peak following [35]

$$I_{(hkl)\alpha} = \frac{I_0 \lambda^3}{64\pi r} r_e^2 \frac{M_{(hkl)}}{V_\alpha^2} \left| F_{(hkl)\alpha} \right|^2 \left(\frac{1 + cos^2(2\theta) cos^2(2\theta_0)}{sin^2\theta cos\theta} \right)_{hkl} \frac{v_\alpha}{\mu_s}, \quad (1)$$

where α refers to a specific phase, hkl represents the Miller indices of a given reflection, I_0 is the incident beam intensity, r is the sample to detector distance, λ is the wavelength, r_e is the classical electron radius, μ_s is the sample's linear attenuation coefficient, v_α = volume fraction of phase α, $M_{(hkl)}$ is the multiplicity for reflection hkl, V_α is the volume of the unit cell of phase α, the fraction in parentheses represents the Lorentz and polarization corrections, 2θ is the diffraction angle, $2\theta_0$ is the monochromator diffraction angle, and $F_{(hkl)\alpha}$ is the structure factor for reflection hkl.

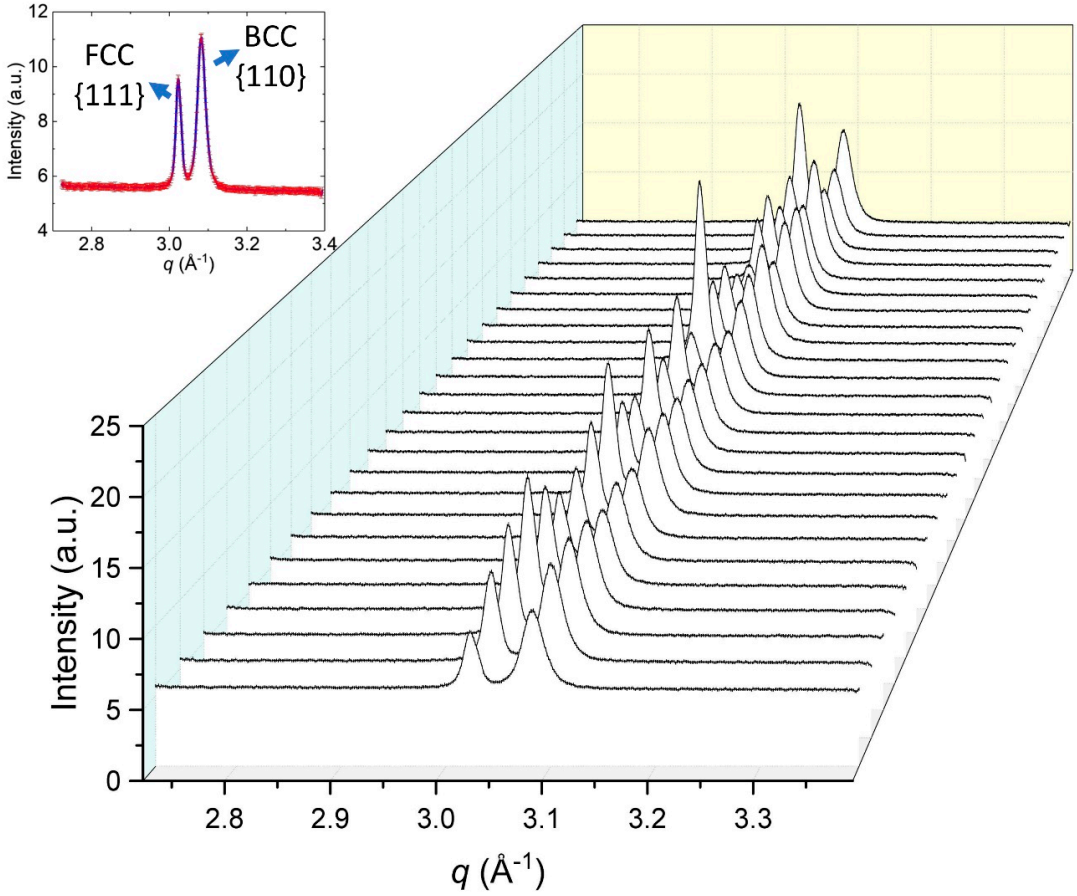

Figure 3. Spatially resolved, in-house XRD data of as-built 17-4 sample with a finely polished surface. For clarity, only the data within a q range of 2.7 $Å^{-1}$ and 3.4 $Å^{-1}$ are shown. The inset shows the indexing of these two peaks as FCC {111} and BCC {110}, respectively.

For a system that contains two phases (austenite, γ and martensite, m), we have

$$\frac{I_{(hkl)\gamma}}{I_{(hkl)m}} = \frac{M_{(hkl)\gamma}{V_m}^2}{M_{(hkl)m}V_\gamma^2}\frac{\left|F_{(hkl)\gamma}\right|^2}{\left|F_{(hkl)m}\right|^2}\frac{\left(\frac{1+cos^2(2\theta)cos^2(2\theta_0)}{sin^2\theta cos\theta}\right)_{(hkl)\gamma}}{\left(\frac{1+cos^2(2\theta)cos^2(2\theta_0)}{sin^2\theta cos\theta}\right)_{(hkl)m}}\frac{v_\gamma}{v_m} \quad (2)$$

Thus, after determining the lattice constants, peak positions in 2θ, and peak integrated intensities, we can calculate $M_{(hkl)}$, V, $F_{(hkl)}$ and use these parameters to determine the phase fractions.

We focused on the austenite {111} peak and martensite {110} peak for the peak fraction analysis. The reasons are two-fold. First, these two peaks are the most intensive peaks for their respective phases. Second, and more importantly, the diffraction angles of these two peaks are very close (only 1° apart in 2θ with Cu Kα radiation), which means that they are probing an almost identical sample volume, for reasons that will be stated in more detail later in this work. The parameters used for phase fraction analysis are listed in Table 2. The lattice parameters were determined using GSAS-II and the integrated peak intensity was automatically determined in batch mode using *Irena*.

Figure 4a–c shows the position-dependent austenite lattice parameter, martensite lattice parameter, and austenite phase fraction for the finely polished sample, respectively. Significant variations in all three sets of values are observed. Phase fraction of austenite, the main topic of this work, was found to be in a range of ≈ 12% to ≈ 45%Moreover, the lattice parameters of these two phases appear to be closely correlated. In other words, at the measurement positions where martensite lattice parameter is high, austenite lattice parameter

is likely high. A statistical analysis shows martensite lattice parameter is (2.880 ± 0.002) Å and the austenite lattice parameter is (3.598 ± 0.002) Å. Here and hereafter, the uncertainty represents one standard deviation. The range of variation, defined as (maximum lattice parameter–minimum lattice parameter)/average lattice parameter, is almost identical for both martensite and austenite at 0.0047. Assuming a Young's modulus at 200 GPa, without considering compositional effect on the lattice parameter measurements, this result suggests a maximum range of stress variation of 970 MPa among all the sample positions, qualitatively in agreement with a recent investigation on cutting and polishing on surface stress of 304 steels at ≈740 MPa [36]. The results acquired on all sample conditions are reported in Table 3.

Table 2. Parameters used to calculate the intensity normalization factors for austenite {111} peak and martensite {110}. The meanings of the parameters are explained in the text associated with Equations (1) and (2).

	h	k	l	Multiplicity	$\lvert F_{hkl} \rvert^2$	2θ_Si(111)	2θ	V (Å^3)	LP Factor	Intensity Normalization Factor
Austenite	1	1	1	8	4642.1	28.44	43.51	46.64	11.85	202.3
Martensite	1	1	0	12	1132.6	28.44	44.55	23.73	11.23	271.2

The average phase fractions of the same part with three different surface conditions are shown in Figure 5. Data clearly indicate that, despite the same austenite phase fraction being expected, the statistically meaningful results strongly depend on the surface finish. The as-cut condition shows (63.3 ± 7.7)% austenite, which more than doubles those fractions acquired under 800 grit and finely polished conditions. While spatial heterogeneity might be able to explain the variations among individual locations, statistically, these differences are significant and show that in-house XRD is not a reliable method to provide quantitative characterization of the austenite fraction in AM 17-4.

Similar conclusions can be drawn for EBSD, an orthogonal, yet commonly used method to characterize phase fraction. The results acquired on two different sample conditions are shown in Figure 6. In both cases, similar to in-house XRD, only martensite and austenite were identified, with the blue region indicating martensite and the yellow region indicating austenite. In Figure 6a, acquired with the sample prepared by polishing alone, EBSD shows almost no presence of austenite (≈0.05% based on area analysis). On the same surface, with an additional two-step ion milling, EBSD under identical measurement conditions shows an austenite level at 40.5%. Ion milling, through atom sputtering, is known to facilitate sample preparation for EBSD measurements and allows the microstructures buried beneath the very top surface layer, such as the Beilby layer, to be observed [37,38]. The difference between these two sets of EBSD results, therefore, strongly indicates the presence of a deformed layer after mechanical polishing.

EBSD and in-house XRD measurements, together, cover a broad range of austenite fraction from 0.05% to ≈76 % (maximum austenite fraction from 75 measurements). This, while not completely reproducing the range of austenite phase fraction covered in Figure 1, does show that common in-house measurements can lead to severe uncertainties. We note that both EBSD and XRD measurements conducted in Bragg–Brentano geometry make use of diffractions by crystallites near surface. This promotes a question—what is the bulk behavior of the same material?

To answer this question, we conducted synchrotron-based HEXRD measurements. A typical dataset is shown in Figure 7. On a linear scale, the acquired HEXRD data show a perfect match with the stick pattern simulated with a Fm-3m symmetry and a lattice constant of (3.5997 ± 0.0004) Å, hence, suggesting the material is (almost) fully austenite. A careful inspection on a linear-log scale, however, shows that a small fraction of martensite exists, as highlighted by the inset of Figure 7. A quantitative analysis of the HEXRD data shows that austenite phase fraction is approximately 99.4%, in other words, consistent with the neutron diffraction results by [33], the only bulk measurement shown in Figure 1.

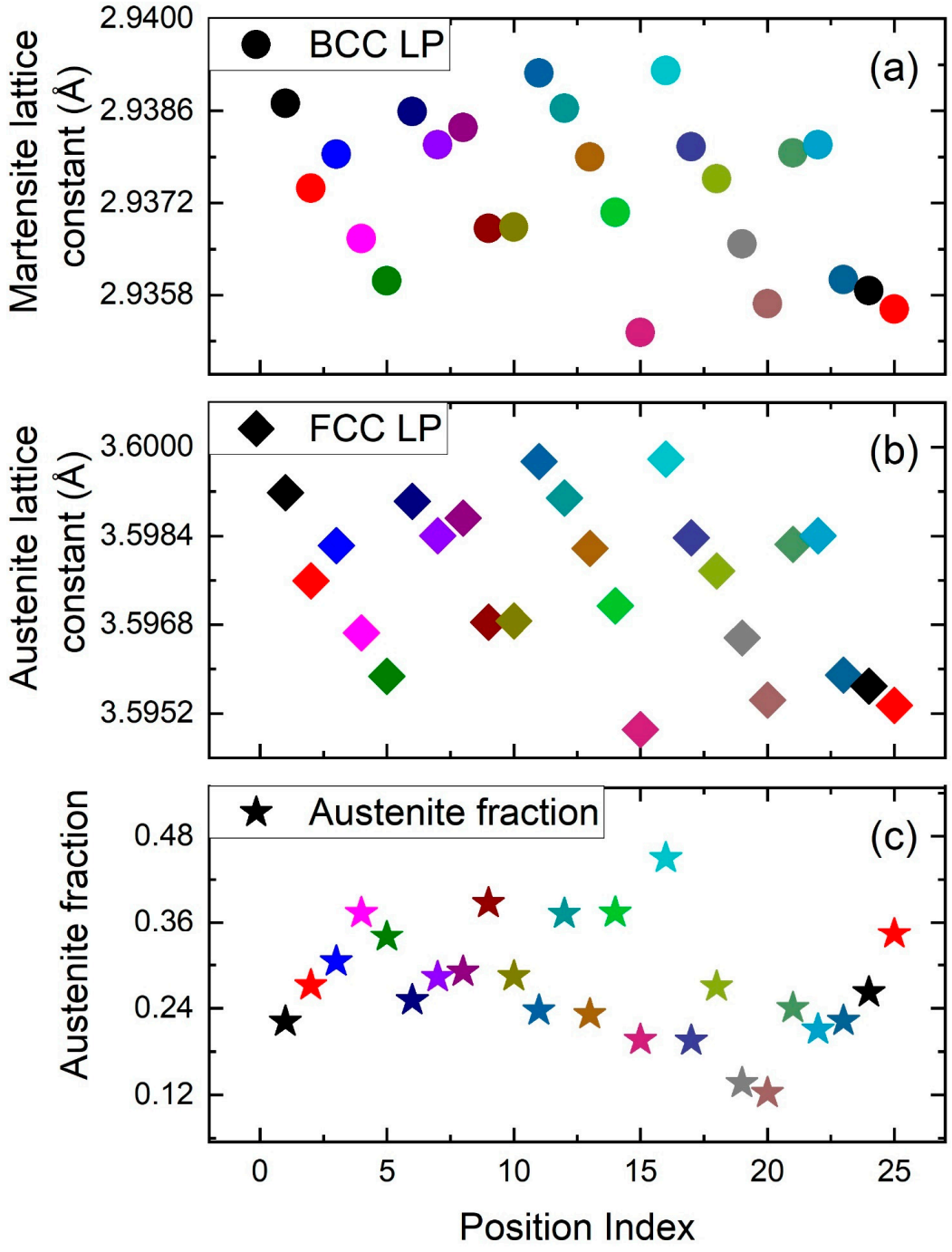

Figure 4. Location-specific (**a**): BCC (martensite) lattice parameter, (**b**): FCC (austenite) lattice parameter, and (**c**): austenite fraction of the 17-4 sample with finely polished surface. The position indices are the same as specified in Figure 2.

Table 3. Statistical austenite lattice parameter, martensite lattice parameter, and austenite fraction from in-house XRD measurements. The uncertainties are reported in one standard deviation.

Heading	Austenite Lattice Parameter (Å)	Martensite Lattice Parameter (Å)	Austenite Fraction
As-cut	3.587 ± 0.003	2.871 ± 0.002	0.633 ± 0.077
800 grit	3.597 ± 0.003	2.881 ± 0.003	0.298 ± 0.039
Finely polished	3.598 ± 0.002	2.880 ± 0.002	0.275 ± 0.080

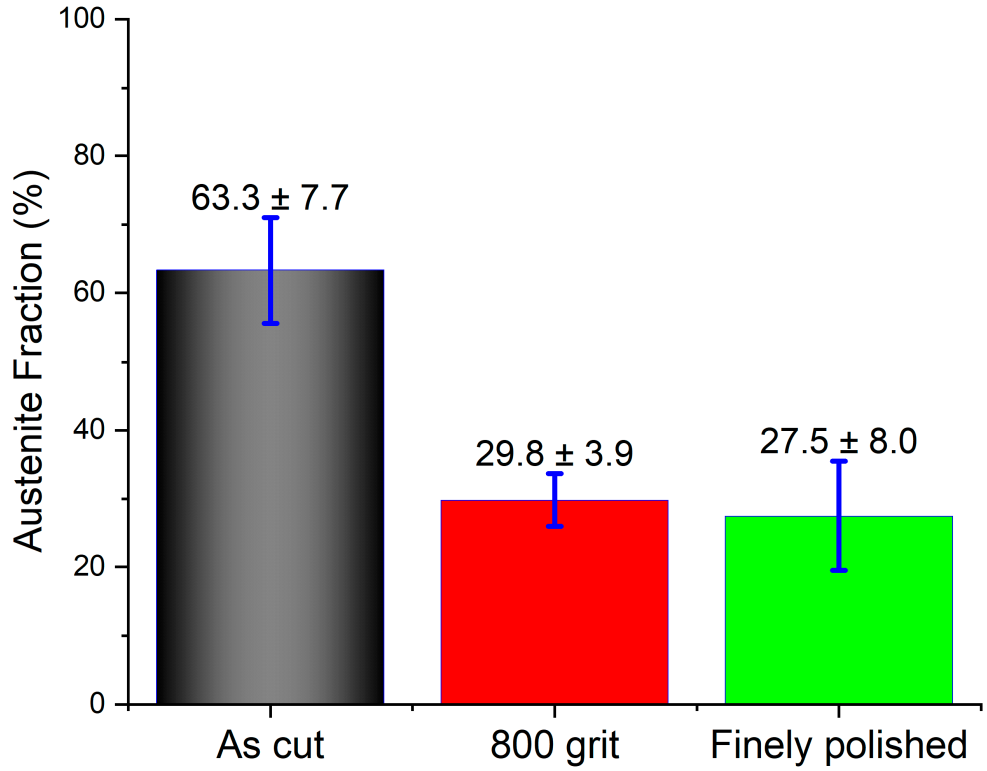

Figure 5. Retained austenite fractions analyzed using 25 sets of XRD data acquired from the same AM 17-4 part with three different surface finishes. "As cut" refers to the unpolished surface after cut using a low-speed saw. "800 grit" refers to a surface polished with an 800-grit sandpaper disc. "Fine polished" refers to a mirror-finish surface prepared following the steps described in the paper. The uncertainties are reported in one standard deviation.

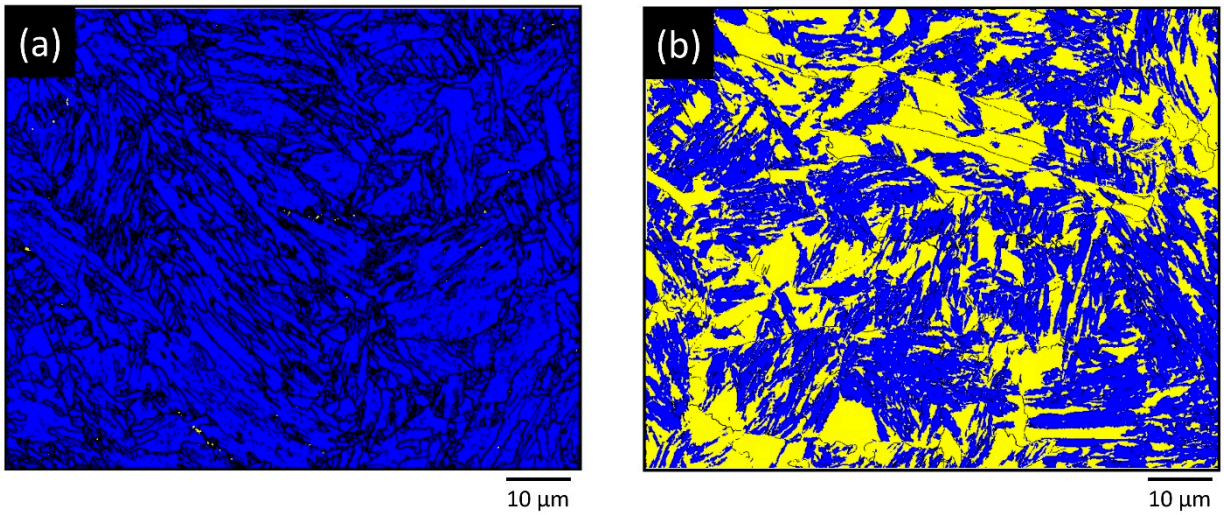

Figure 6. EBSD data on the same 17-4specimen with two different surface finishes. (**a**). Mechanical polish to 1 µm, followed by a 16 h vibratory polishing step using colloidal SiC. (**b**) The same polish steps as (**a**), followed by two ion mill steps. The first step was 30 min at 400 V, 7 mA and the second step was 40 min at 200 V, 2 mA. In both (**a**,**b**), blue region indicates martensite and yellow region indicates austenite.

An individual may wonder, for two pieces of AM 17-4 alloy cut from the same part, using the same characterization technique (X-ray diffraction), why the results from in-house measurements differ so much from HEXRD results. The answer, as inferred above, lies in the diffraction geometry. This is explained in Figure 8.

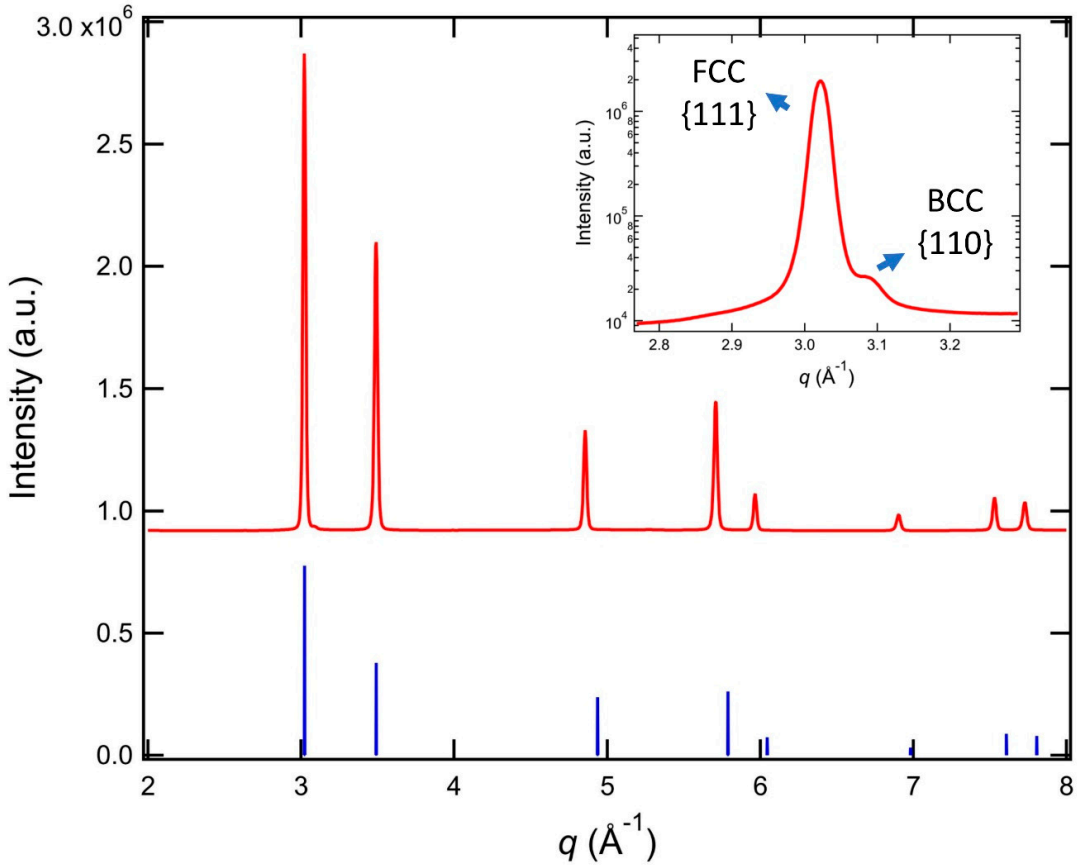

Figure 7. Synchrotron-based HEXRD of 1 mm thick as-built AM 17-4. The stick pattern was calculated with a Fm-3m symmetry and a lattice constant of 3.5997 Å. The inset shows the same XRD pattern, with the intensity on a logarithmic scale to highlight the presence of very weak BCC peaks.

The sample volume probed by XRD in the Bragg–Brentano geometry, as in the case of the typical in-house X-ray diffractometer, depends on the sample penetration because of X-ray absorption. As an X-ray photon is absorbed by an atom, the excess energy is transferred to an electron. This creates a photoelectric absorption process, which is quantitatively described by a linear absorption coefficient. It is well known [39] that, for an incident beam intensity of I_0, after transmitting a distance z in a material with linear absorption coefficient μ, the transmitted intensity becomes

$$I = I_0 \exp(-\mu z) \tag{3}$$

In a reflection geometry, as depicted by the inset of Figure 8, for a diffraction angle of 2θ, and total X-ray travel distance z, the penetration depth d is simply

$$d = -\ln\left(\frac{I}{I_0}\right) sin(\theta)/2\mu \tag{4}$$

For simplicity, we calculated the linear transmission coefficient of Cu Kα X-rays (wavelength 1.5418 Å) in Fe (density 7.874 g/cm^3) at 2363 cm^{-1} using *Irena* [16]. Assuming a 5% transmission (I/I_0), we calculated the diffraction angle-dependent penetration depth for Cu Kα X-rays. This is shown in Figure 8. There are two main conclusions which can be drawn. First, Cu Kα X-rays only penetrate the first few micrometers of the surface. Therefore, the in-house X-ray results are strictly surface-sensitive. This conclusion is not limited to Fe (steel). For metallic materials that contain a significant fraction of heavy elements, most in-house X-ray diffractometers equipped with common X-ray sources, such as Cu, Mo, and Co, only probe surface and near-surface crystal structures. Using the same

X-ray source, in general, the denser the material, the less the penetration depth. Table 4 summarizes the calculated penetration depths at 5% penetration for Fe, Ni, Al, Co, and Cu, for in-house XRD diffractometers using a Cu Kα source in a Bragg–Brentano (reflection) geometry. We found that for the {111} reflection of their respective diffraction patterns, the penetration depths range from 2 μm to 38 μm, i.e., either on surface or near surface. Second, XRD data at different diffraction angles are acquired from different sample volumes, due to both different penetration depths and different incident X-ray footprints, which adds additional complexity for quantitative analysis. This also explains why we focused on austenite {111} and martensite {110} peaks for quantitative phase fraction analysis in this study, as they are closely positioned and probe almost identical sample volume.

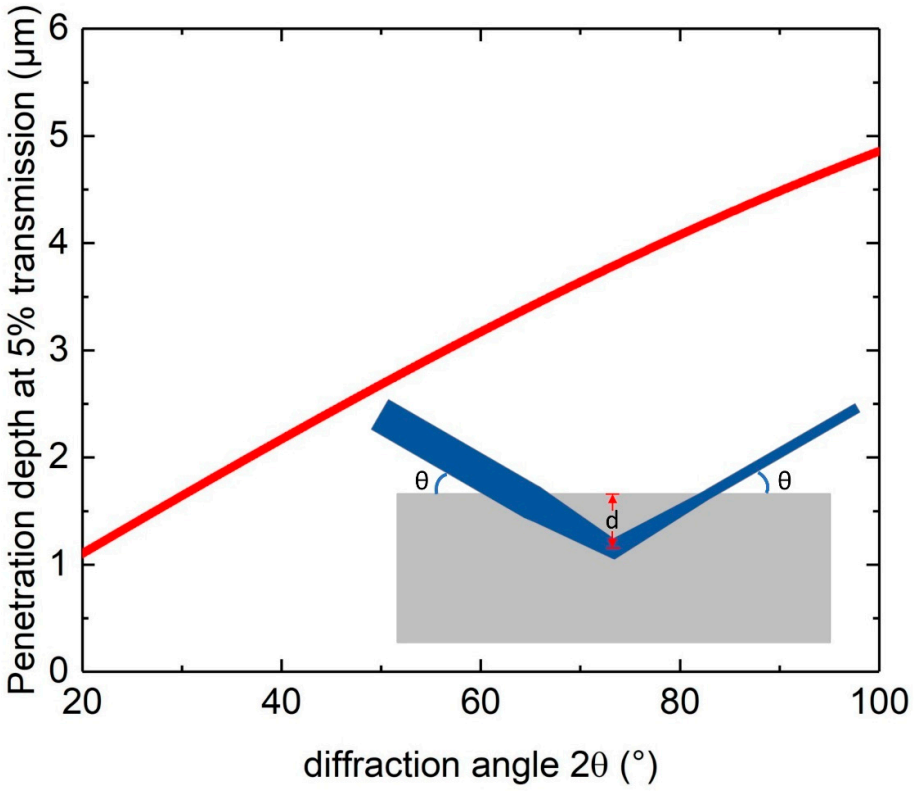

Figure 8. Diffraction-angle dependent penetration depth of Cu Kα X-rays in Fe. The absorption threshold was set at 95 %. The schematic in the inset illustrates the Bragg–Brentano geometry. The width of the beam indicates the number of X-ray photons transmitted.

Table 4. Calculated penetration depths at 5% penetration (I/I_0, as in Equation (4)) for Fe, Ni, Al, Co, and Cu, for in-house XRD diffractometers using a Cu Kα source in a Bragg–Brentano (reflection) geometry. These values also serve as ballpark guidance for Fe, Ni, Al, Co, and Cu alloys.

	Density (g/cm^3)	Absorption Coefficient (cm^{-1})	FCC Lattice Parameter (Å)	2θ Angle for {111} Reflection (°)	Penetration Depth (μm)
Fe	7.9	2363	3.555	44.12	2.4
Ni	8.9	405	3.499	44.87	14.1
Al	2.7	129	4.046	38.54	38.3
Co	8.9	2863	3.544	44.27	2.0
Cu	9.0	436	3.597	43.58	12.8

Electrons, when compared with X-rays, have significantly less penetration power because of electron's much higher scattering cross-section. In steel, previous Monte Carlo

simulations [40] and experimental work [41] have suggested that the EBSD's penetration depth is on the scale of 25 nm, i.e., two orders of magnitude lower than in-house XRD. This makes EBSD even more surface-sensitive and explains the drastic differences observed in this study on the same 17-4 mechanically polished surface before and after a two-step ion milling treatment.

Our in-house XRD and EBSD results both firmly point to the role of surface finish on the acquired phase fractions in as-built AM 17-4. The main purpose of polishing is to remove surface irregularities and reduce surface roughness. However, it has been long recognized that polishing can also introduce a surface layer with an altered microstructure [42–45]. New insight gained from electron microscopy and asperity-abrasive contact further suggests that during polishing, repetitive sliding contacts allow the surface asperities to undergo plastic flow and introduce plastic deformation in a thin (1 μm–10 μm) layer at the top of an AM Ti-6Al-4V alloy surface [46]. In other words, normal polishing methods create a deformation layer with a layer thickness that covers the penetration depth of typical in-house XRD and EBSD for many types of alloys, and can lead to undesirable repercussions for the measurement results.

This type of plastic deformation creates a challenge for phase fraction analysis of alloys such as 17-4. The metastable austenite in 17-4 formed during AM processing is known to be associated with a high stacking-fault probability with a stacking fault energy on the scale of 15–20 mJ m^{-2} [35]. Austenite with this type of thermodynamic instability can transform to martensite during loading or deformation, because the applied stress acts to provide the energy necessary to transform austenite to martensite at a temperature above the martensite start temperature Ms. This resembles the strengthening mechanism in typical TRIP (transformation-induced plasticity) steels [47,48]. In AM 17-4, deformation-induced austenite–martensite transformation, including complete transformation, has been reported [32,49]. This suggests that, polishing-induced, near-surface structural transformation from the metastable austenite to martensite creates a situation that makes reliable phase-fraction determination using in-house XRD and EBSD measurements very difficult, if not impossible.

Synchrotron-based HEXRD, on the other hand, was conducted in the transmission geometry, where high energy X-ray was able to penetrate 1 mm thick steel due to its much smaller absorption coefficient–X-ray absorption coefficient μ is 2363 cm^{-1} at 8.04 keV (Cu Kα) vs. 8.1 cm^{-1} at 58.68 keV (the X-ray energy for the HEXRD measurements). The HEXRD specimen, after cutting, was polished on both sides, which created the same type of damage layers for HEXRD as for in-house XRD and EBSD. However, because the sample volume that was subject to the deformation-induced transformation was relatively small (damage fraction is on the scale of 2 × 10 μm/1 mm = 0.02 or smaller), the impact of this sample-preparation related uncertainty is therefore much less significant. This is reflected in the 99.4% austenite volume fraction acquired from the HEXRD analysis, which effectively suggests that the as-built AM 17-4 used in this study is close to being fully austenitic. Interestingly, our HEXRD measurements on the virgin GP1 powder show an austenite fraction of 0.797 (data not shown). This indicates that the solidification process during build dictates the phase landscape of the as-built AM 17-4.

The 17-4 is designed as a martensitic steel, with an Ms temperature at ≈130 °C [1,50]. Yet our results show that the as-built AM 17-4 is approximately 100% austenite. To rationalize this extreme difference, we conducted comprehensive modeling studies to understand the solidification behavior and solid-state transformation of AM 17-4. Some of the results are reported in Figure 9.

Figure 9a shows the solidification behavior of 17-4. A total of three different approaches were applied, namely, equilibrium solidification, Scheil solidification, and DICTRA solidification. Equilibrium solidification followed the equilibrium phase diagram, where solid state diffusion is complete. Scheil solidification assumes perfect mixing in the liquid and ignores diffusion in the solid phase. DICTRA solidification considers diffusion in the liquid and solid phases, which both contribute to mass redistribution, and therefore

accounts for temperature-dependent elemental diffusion and partitioning and more closely resembles the physical reality. The DICTRA simulation starts at a high temperature when only the liquid phase is present, as cooling proceeds the two stable phases (FCC and BCC) are introduced from the sides as per an eutectic reaction." The solidified material during AM is heated again as scanning proceeds, and this stepwise heating must be considered to obtain a more realistic model. In this process, we assume cooling is conducted until the material is fully solidified and undergoes a heating at 1×10^6 °C/s to account for a second scan and its associated cooling thereafter. As the material is layered, heat is conducted to the already solidified material. A third heating and cooling is also included during the simulation, however at lower temperature as the heat conducted after the third layer is less. This approach is similar to the thermal history reported previously [51].

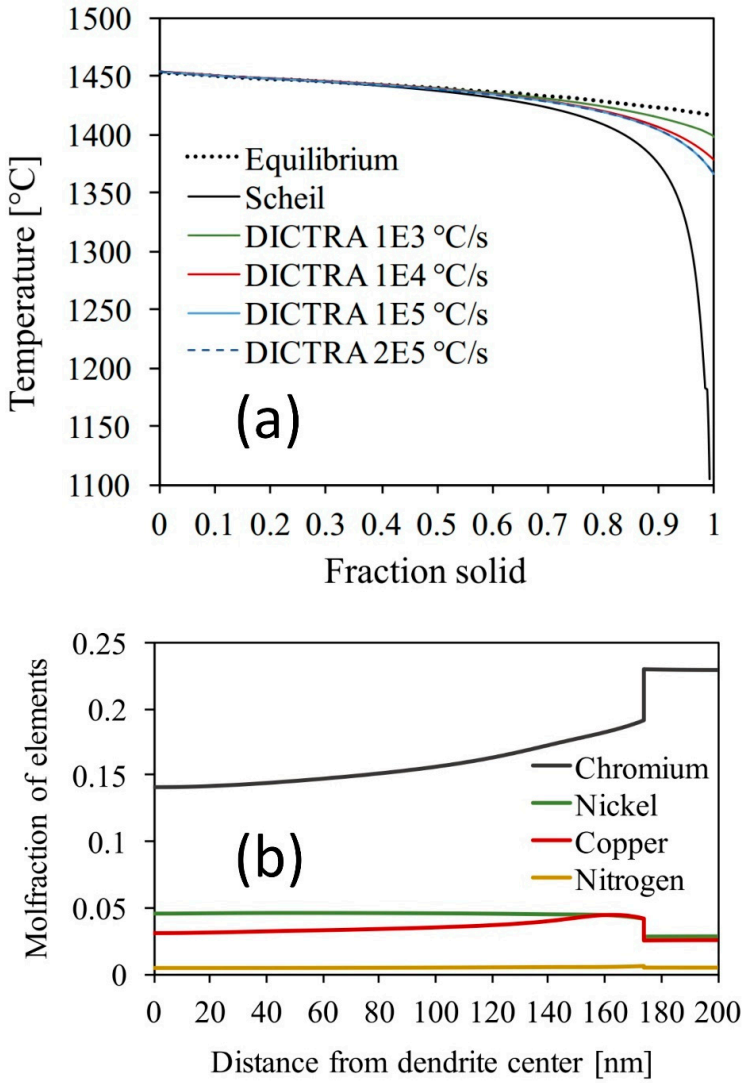

Figure 9. (**a**) Temperature-dependent solidification profile for reduced composition of 17-4 using equilibrium solidification, Scheil solidification, and DICTRA at different cooling rates. (**b**): elemental distribution across dendritic arm spacing predicted by DICTRA at a cooling rate of 1×10^5 °C/s.

In DICTRA simulation, cooling rates from 1×10^3 °C/s to 2×10^5 °C/s were considered. These cooling rates are commonly encountered in directed energy deposition and laser powder-bed fusion-based AM processing. It is clear from Figure 9a that, as expected, equilibrium solidification and Scheil solidification represented the two extremes (theoretical limits), and the more physically reasonable DICTRA simulations fall in-between because they use both thermodynamic and kinetic data for diffusion calculations. Predic-

tion made by Scheil simulations, in particular, shows significant deviation from DICTRA results, evidenced by the greater than 200 °C difference in fully solidified temperature. This suggests that Scheil simulation, despite its simplicity and availability [52], may not be a good approximation for the AM solidification process in 17-4. It is also evident that the fully solidified temperature (where fraction solid = 1) is cooling rate dependent—the higher the cooling rate, the lower the temperature.

To emulate the real AM processing condition, we adopted a 3-pass thermal history similar to the one applied in Keller et al., which was determined by finite element analysis and validated by thermographic measurements [51]. Assuming one half of the interdendritic distance of 200 nm, DICTRA simulation at a cooling rate of 1×10^5 °C/s predicted a segregation profile, as shown in Figure 9b. An abrupt jump in the molar fraction of Cr, Ni, and Cu was observed at ≈175 nm. Interestingly, this prediction is consistent with previous observations by Cheruvathur et al. [28] in as-built 17-4, where they reported that Fe and Cr are enriched in the dendritic cores. Because these elements have a different solubility in the FCC austenite phase and BCC ferrite phase, this suggests that high temperature δ ferrite may remain upon solidification, through a solidification-velocity dependent competition between austenite and δ ferrite [53]. Recent synchrotron-based high-speed X-ray diffraction experiments that follow the solidification phase transformation sequence from melt to room temperature convincingly demonstrate that the high-temperature δ ferrite, once formed, can sustain to room temperature, albeit at a reduced phase fraction at room temperature than at solidus [54]. We emphasize that the phase fraction indicated by Figure 9b is qualitative as it represents only a line, instead of volumetric, profile. In addition, further cooling leads shifts in Gibbs energy curves and fraction of FCC austenite is expected to increase, hence serving to reduce the volume fraction of high-temperature δ ferrite even further (at this composition).

The as-solidified microstructure serves as a starting point for the solid-state transformation of as-built AM 17-4. It has been well established that nitrogen is highly effective (20 × more effective than Ni) in stabilizing austenite and reducing the tendency for martensitic transformation to lower temperatures [55]. In AM 17-4 literature, nitrogen stabilization is also identified as the main mechanism for the reduction of the Ms in nitrogen atomized 17-4 [31]. Using the compositional profiles acquired in Figure 9b, we calculated the Cr-Ni contour maps for the Ms with and without nitrogen. Our results, which will be reported in detail elsewhere, show that a reduction in the Ms temperature by over 100 °C when 0.12% mass nitrogen is present and that the lath Ms is below 0 °C. This is consistent with the experimental evidence that a quench to −40 °C is required to recover a nearly fully (≈95%) martensitic structure in nitrogen atomized 17-4 [31]. This significant reduction in Ms, from another angle, corroborates our finding that our AM 17-4 is indeed almost fully austenitic in its as-built state and that a bulk measurement technique is required to quantitively characterize the phase fractions.

Previous works have suggested that for AM 17-4, post-build treatment can be effective to recover the martensitic microstructure of wrought 17-4 [26,31]. While this is clearly feasible, evidence used to support this argument is oftentimes obtained with surface-based analytical techniques such as XRD with Cu or Mo source and SEM. With the uncertainties associated with these approaches, as is clearly demonstrated in our results, we argue that special attention must be given to establish the effectiveness of post-build treatment protocols for AM 17-4 and similar alloys, so that the perceived martensitic structure after post-build heat treatment is indeed the desired microstructure. For example, using Cu Kα X-ray, Lebrun et al. reported that a heat treatment (1040 °C for 30 min) followed by cooling to room temperature completely transforms their 17-4 to 100% martensite, where the martensitic start and finish temperatures were estimated at 100 °C and 32 °C, respectively. Conversely, in a separate study, using synchrotron high-energy XRD, Lass et al. found that a cooling step to −40 °C and lower, after heat treatment at elevated temperatures (1150 °C for 1 h and 1050 °C for 30 min), is necessary to convert their AM 17-4 to a ≈95% martensitic structure, suggesting the martensitic finish temperature is well below room

temperature. Such differences cannot be ignored, as the strength of 17-4 originates from both the martensites and the Cu precipitates. Thus, the identification of the correct heat treatment procedure that can truly recover the martensitic structure serves as the starting point of an aging heat treatment that seeks to optimize the mechanical property of this class of important AM alloy.

4. Conclusions

Phase fraction analysis is a routine element of microstructural analysis of AM alloys. The 17-4 precipitation-hardening martensitic stainless steel, as an important class of AM alloy, has received broad attention within the AM research community. The reported phase fractions of as-built AM 17-4, however, show significant variation.

We conducted a careful study to understand this variation, making use of widely available in-house XRD and EBSD and less accessible high-energy X-ray diffraction, as well as Calphad modeling. Our in-house XRD measurements were conducted on the same AM part with three different surface finishes. On each surface, we measured 25 sample positions. The in-house XRD measurements show strong dependence on the measurement positions. Statistically significant differences were identified on the austenite fractions acquired on three surface finishes. Our results also suggest surface stress variation on the scale of 900 MPa may exist on these samples. Similar results were acquired using EBSD measurements, where a fully martensitic microstructure was observed on a mechanically polished surface.

The bulk measurements conducted with high-energy X-ray diffraction tell a different story. The as-built AM 17-4 specimen prepared using the same AM part consists of nearly 100% austenite, which is corroborated by our Calphad modeling results. Our analyses show that for alloys with heavy elements, in-house XRD and EBSD are strictly surface sensitive techniques with different degree of penetration power (in-house XRD using Cu source, a few micrometers; EBSD, tens of nanometers). Hence, measurements made using these techniques must be understood in their correct context.

Our results have significant implications because 17-4, as designed, is a martensitic steel with superior strength. While it is known that retained austenite exists in AM as-built 17-4, it remains a collective goal in the AM steel community to either identify an effective heat treatment procedures to recover the martensitic microstructure or optimize the alloy composition and/or build parameters to achieve a martensitic structure in the as-built state. In other words, a martensitic microstructure is required before the ageing step that promotes the formation of Cu precipitates and further strengthening of the alloy can take place. An accurate evaluation of the phase fraction is therefore crucial in determining the efficacy of heat treatment procedures or composition and build-parameter optimization.

In a more general sense, our findings unequivocally demonstrate that, for AM alloys that are prone to plastic deformation-induced structure transformation, careful consideration of surface-sensitive characterization techniques such as in-house XRD or EBSD must be given. Characterizations with less accessible but bulk sensitive techniques such as synchrotron-based high energy X-ray diffraction or neutron diffraction may be required.

Author Contributions: Conceptualization, F.Z. and M.R.S.; X-ray measurements: F.Z. and M.E.W.; CALPHAD, S.H., E.A.L., and C.E.C.; SEM, M.R.S. and M.E.W.; X-ray analysis, F.Z.; data curation, F.Z., M.R.S. and S.H.; writing—original draft preparation, F.Z.; writing—review and editing, all authors; project administration, F.Z. All authors have read and agreed to the published version of the manuscript.

Funding: This research received no external funding.

Data Availability Statement: Data are available upon request.

Acknowledgments: Use of the Advanced Photon Source, an Office of Science User Facility operated for the U.S. Department of Energy (DOE) Office of Science by Argonne National Laboratory, was supported by the U.S. DOE under Contract No. DE-AC02–06CH11357.

Conflicts of Interest: The authors declare no conflict of interest.

References

1. Campbell, C.E.; Stoudt, M.R.; Zhang, F. Additive manufacturing of steels and stainless steels. In *Additive Manufacturing Processes*; Bourell, D.L., Frazier, W., Kuhn, H., Seifi, M., Eds.; ASM International: Materials Park, OH, USA, 2020.
2. Tofail, S.A.; Koumoulos, E.P.; Bandyopadhyay, A.; Bose, S.; O'Donoghue, L.; Charitidis, C. Additive manufacturing: Scientific and technological challenges, market uptake and opportunities. *Mater. Today* **2018**, *21*, 22–37. [CrossRef]
3. Pereira, T.; Kennedy, J.V.; Potgieter, J. A comparison of traditional manufacturing vs additive manufacturing, the best method for the job. *Procedia Manuf.* **2019**, *30*, 11–18. [CrossRef]
4. Khorasani, M.; Ghasemi, A.; Rolfe, B.; Gibson, I. Additive manufacturing a powerful tool for the aerospace industry. *Rapid Prototyp. J.* **2021**. [CrossRef]
5. Okamoto, H.; Schlesinger, M.E.; Mueller, E.M. *Alloy Phase Diagrams*; ASM International: Materials Park, OH, USA, 2016.
6. Xu, W.; Brandt, M.; Sun, S.; Elambasseril, J.; Liu, Q.; Latham, K.; Xia, K.; Qian, M. Additive manufacturing of strong and ductile Ti–6Al–4V by selective laser melting via in situ martensite decomposition. *Acta Mater.* **2015**, *85*, 74–84. [CrossRef]
7. Facchini, L.; Vicente, N.; Lonardelli, I.; Magalini, E.; Robotti, P.; Molinari, A. Metastable Austenite in 17-4 Precipitation-Hardening Stainless Steel Produced by Selective Laser Melting. *Adv. Eng. Mater.* **2010**, *12*, 184–188. [CrossRef]
8. Alam, M.K.; Mehdi, M.; Urbanic, R.J.; Edrisy, A. Mechanical behavior of additive manufactured AISI 420 martensitic stainless steel. *Mater. Sci. Eng. A* **2020**, *773*, 138815. [CrossRef]
9. Lehnert, R.; Wagner, R.; Burkhardt, C.; Clausnitzer, P.; Weidner, A.; Wendler, M.; Volkova, O.; Biermann, H. Microstructural and mechanical characterization of high-alloy quenching and partitioning TRIP steel manufactured by electron beam melting. *Mater. Sci. Eng. A* **2020**, *794*, 139684. [CrossRef]
10. Zhang, F.; Levine, L.E.; Allen, A.J.; Stoudt, M.R.; Lindwall, G.; Lass, E.A.; Williams, M.E.; Idell, Y.; Campbell, C.E. Effect of heat treatment on the microstructural evolution of a nickel-based superalloy additive-manufactured by laser powder bed fusion. *Acta Mater.* **2018**, *152*, 200–214. [CrossRef] [PubMed]
11. Stoudt, M.R.; Lass, E.; Ng, D.S.; Williams, M.E.; Zhang, F.; Campbell, C.E.; Lindwall, G.; Levine, L.E. The Influence of Annealing Temperature and Time on the Formation of δ-Phase in Additively-Manufactured Inconel 625. *Met. Mater. Trans. A* **2018**, *49*, 3028–3037. [CrossRef]
12. Raghavan, S.; Zhang, B.; Wang, P.; Sun, C.-N.; Nai, M.L.S.; Li, T.; Wei, J. Effect of different heat treatments on the microstructure and mechanical properties in selective laser melted INCONEL 718 alloy. *Mater. Manuf. Process.* **2016**, *32*, 1588–1595. [CrossRef]
13. Zuback, J.; Moradifar, P.; Khayat, Z.; Alem, N.; Palmer, T. Impact of chemical composition on precipitate morphology in an additively manufactured nickel base superalloy. *J. Alloys Compd.* **2019**, *798*, 446–457. [CrossRef]
14. Zhang, F.; Ilavsky, J.; Lindwall, G.; Stoudt, M.R.; Levine, L.E.; Allen, A.J. Solid-State Transformation of an Additive Manufactured Inconel 625 Alloy at 700 °C. *Appl. Sci.* **2021**, *11*, 8643. [CrossRef]
15. Di Schino, A. Manufacturing and Applications of Stainless Steels. *Metals* **2020**, *10*, 327. [CrossRef]
16. Ilavsky, J.; Jemian, P.R. Irena: Tool suite for modeling and analysis of small-angle scattering. *J. Appl. Crystallogr.* **2009**, *42*, 347–353. [CrossRef]
17. Toby, B.; Von Dreele, R.B. GSAS-II: The genesis of a modern open-source all purpose crystallography software package. *J. Appl. Crystallogr.* **2013**, *46*, 544–549. [CrossRef]
18. Borkiewicz, O.J.; Ruett, U.; Beyer, K.; Gallington, L. New capabilities at beamline 11-ID-B of the Advanced Photon Source. *Acta Crystallogr. Sect. A Found. Adv.* **2019**, *75*, a352. [CrossRef]
19. Cline, J.; Filliben, J.; Von Dreele, R.; Winburn, R.; Stephens, P. D-90 Addressing the Amorphous Content Issue in Quantitative Phase Analysis: The Certification of NIST SRM 676A. *Powder Diffr.* **2009**, *24*, 172. [CrossRef]
20. Andersson, J.-O.; Helander, T.; Höglund, L.; Shi, P.; Sundman, B. Thermo-Calc & DICTRA, computational tools for materials science. *Calphad* **2002**, *26*, 273–312. [CrossRef]
21. Gulliver, G. The quantitative effect of rapid cooling upon the constitution of binary alloys. *J. Inst. Met.* **1913**, *9*, 120–157.
22. Steels, T.-T. *Fe-Alloys Database Version 7.0*; Thermo-Calc Software: Solna, Sweden, 2012.
23. Liu, S.; Shin, Y.C. Additive manufacturing of Ti6Al4V alloy: A review. *Mater. Des.* **2019**, *164*, 107552. [CrossRef]
24. Popovich, V.; Borisov, E.; Sufiiarov, V.; Masaylo, D.; Alzina, L. Functionally graded Inconel 718 processed by additive manufacturing: Crystallographic texture, anisotropy of microstructure and mechanical properties. *Mater. Des.* **2017**, *114*, 441–449. [CrossRef]
25. Jia, Q.; Zhang, F.; Rometsch, P.; Li, J.; Mata, J.; Weyland, M.; Bourgeois, L.; Sui, M.; Wu, X. Precipitation kinetics, microstructure evolution and mechanical behavior of a developed Al–Mn–Sc alloy fabricated by selective laser melting. *Acta Mater.* **2020**, *193*, 239–251. [CrossRef]
26. Le Brun, T.; Nakamoto, T.; Horikawa, K.; Kobayashi, H. Effect of retained austenite on subsequent thermal processing and re-sultant mechanical properties of selective laser melted 17–4 ph stainless steel. *Mater. Design* **2015**, *81*, 44–53. [CrossRef]
27. Averyanova, M.; Bertrand, P.; Verquin, B. Effect of initial powder properties on final microstructure and mechanical properties of parts manufactured by selective laser melting. In Proceedings of the Annals of DAAAM for 2010 & Proceedings of the 21st International DAAAM Symposium, Zadar, Croatia, 20–23 October 2010.

28. Cheruvathur, S.; Lass, E.A.; Campbell, C.E. Additive Manufacturing of 17-4 PH Stainless Steel: Post-processing Heat Treatment to Achieve Uniform Reproducible Microstructure. *JOM* **2016**, *68*, 930–942. [CrossRef]
29. Stoudt, M.R.; Ricker, R.E.; Lass, E.; Levine, L.E. Influence of postbuild microstructure on the electrochemical behavior of additively manufactured 17-4 ph stainless steel. *JOM* **2017**, *69*, 506–515. [CrossRef]
30. Meredith, S.; Zuback, J.; Keist, J.; Palmer, T. Impact of composition on the heat treatment response of additively manufactured 17–4 PH grade stainless steel. *Mater. Sci. Eng. A* **2018**, *738*, 44–56. [CrossRef]
31. Lass, E.A.; Zhang, F.; Campbell, C.E. Nitrogen Effects in Additively Manufactured Martensitic Stainless Steels: Conventional Thermal Processing and Comparison with Wrought. *Met. Mater. Trans. A* **2020**, *51*, 2318–2332. [CrossRef]
32. Wang, X.; Liu, Y.; Shi, T.; Wang, Y. Strain rate dependence of mechanical property in a selective laser melted 17–4 PH stainless steel with different states. *Mater. Sci. Eng. A* **2020**, *792*, 139776. [CrossRef]
33. Clausen, B.; Brown, D.; Carpenter, J.; Clarke, K.; Clarke, A.; Vogel, S.; Bernardin, J.; Spernjak, D.; Thompson, J. Deformation behavior of additively manufactured GP1 stainless steel. *Mater. Sci. Eng. A* **2017**, *696*, 331–340. [CrossRef]
34. Zhang, F.; Levine, L.E.; Allen, A.J.; Young, S.W.; Williams, M.E.; Stoudt, M.R.; Moon, K.-W.; Heigel, J.C.; Ilavsky, J. Phase Fraction and Evolution of Additively Manufactured (AM) 15-5 Stainless Steel and Inconel 625 AM-Bench Artifacts. *Integr. Mater. Manuf. Innov.* **2019**, *8*, 362–377. [CrossRef]
35. Lindwall, G.; Campbell, C.; Lass, E.; Zhang, F.; Stoudt, M.R.; Allen, A.J.; Levine, L.E. Simulation of ttt curves for additively man-ufactured inconel 625. *Metall. Mater. Trans. A* **2019**, *50*, 457–467. [CrossRef]
36. Hayashi, M. Residual Stresses Induced by Surface Working and Their Improvement by Emery Paper Polishing. *Quantum Beam Sci.* **2020**, *4*, 21. [CrossRef]
37. Berecz, T.; Kalácska, S.; Varga, G.; Dankházi, Z.; Havancsák, K. Effect of High Energy Ar-Ion Milling on Surface of Quenched Low-Carbon Low-Alloyed Steel. *Mater. Sci. Forum* **2015**, *812*, 285–290. [CrossRef]
38. Mateescu, N.; Ferry, M.; Xu, W.; Cairney, J. Some factors affecting EBSD pattern quality of Ga+ ion-milled face centred cubic metal surfaces. *Mater. Chem. Phys.* **2007**, *106*, 142–148. [CrossRef]
39. Als-Nielsen, J.; McMorrow, D. *Elements of Modern X-ray Physics*; John Wiley & Sons: Hoboken, NJ, USA, 2011.
40. Drouin, D.; Couture, A.R.; Joly, D.; Tastet, X.; Aimez, V.; Gauvin, R. Casino v2. 42—A fast and easy-to-use modeling tool for scanning electron microscopy and microanalysis users. *Scanning J. Scanning Microsc.* **2007**, *29*, 92–101.
41. Plancher, E.; Petit, J.; Maurice, C.; Favier, V.; Saintoyant, L.; Loisnard, D.; Rupin, N.; Marijon, J.-B.; Ulrich, O.; Bornert, M. On the accuracy of elastic strain field measurements by laue microdiffraction and high-resolution ebsd: A cross-validation experiment. *Exp. Mechan.* **2016**, *56*, 483–492. [CrossRef]
42. Lux, G.; Blum, W. Methods of polishing steel and their effects upon the protective value of electroplated coatings. *J. Res. Natl. Inst. Stand. Technol.* **1945**, *34*, 295. [CrossRef]
43. Ma, C.; Han, E.-H.; Peng, Q.; Ke, W. Effect of polishing process on corrosion behavior of 308L stainless steel in high temperature water. *Appl. Surf. Sci.* **2018**, *442*, 423–436. [CrossRef]
44. Aghan, R.; Samuels, L. Mechanisms of abrasive polishing. *Wear* **1970**, *16*, 293–301. [CrossRef]
45. Xie, Y.; Bhushan, B. Effects of particle size, polishing pad and contact pressure in free abrasive polishing. *Wear* **1996**, *200*, 281–295. [CrossRef]
46. Iquebal, A.S.; Sagapuram, D.; Bukkapatnam, S. Surface plastic flow in polishing of rough surfaces. *Sci. Rep.* **2019**, *9*, 1–11. [CrossRef]
47. Harjo, S.; Tsuchida, N.; Abe, J.; Gong, W. Martensite phase stress and the strengthening mechanism in TRIP steel by neutron diffraction. *Sci. Rep.* **2017**, *7*, 1–11. [CrossRef]
48. Martin, S.; Wolf, S.; Martin, U.; Krüger, L.; Rafaja, D. Deformation Mechanisms in Austenitic TRIP/TWIP Steel as a Function of Temperature. *Met. Mater. Trans. A* **2016**, *47*, 49–58. [CrossRef]
49. Phan, T.Q.; Kim, F.H.; Pagan, D.C. Micromechanical response quantification using high-energy x-rays during phase transformations in additively manufactured 17-4 stainless steel. *Mater. Sci. Eng. A* **2019**, *759*, 565–573. [CrossRef]
50. Steel, A. *17-4 ph Stainless Steel: Product Data Bulletin*; AK Steel Corporation: West Chester, OH, USA, 2015.
51. Keller, T.; Lindwall, G.; Ghosh, S.; Ma, L.; Lane, B.M.; Zhang, F.; Kattner, U.R.; Lass, E.A.; Heigel, J.C.; Idell, Y. Application of finite element, phase-field, and calphad-based methods to additive manufacturing of ni-based superalloys. *Acta Mater.* **2017**, *139*, 244–253. [CrossRef] [PubMed]
52. Pasebani, S.; Ghayoor, M.; Badwe, S.; Irrinki, H.; Atre, S.V. Effects of atomizing media and post processing on mechanical properties of 17-4 PH stainless steel manufactured via selective laser melting. *Addit. Manuf.* **2018**, *22*, 127–137. [CrossRef]
53. Chou, C.-Y.; Pettersson, N.H.; Durga, A.; Zhang, F.; Oikonomou, C.; Borgenstam, A.; Odqvist, J.; Lindwall, G. Influence of solidi-fication structure on austenite to martensite transformation in additively manufactured hot-work tool steels. *Acta Mater.* **2021**, *215*, 117044. [CrossRef]
54. Guo, Q.; Qu, M.; Chuang, C.-P.; Xiong, L.; Young, Z.A.; Zhang, F.; Chen, L. Phase transformation dynamics informed alloy design for additive manufacturing. *Acta Mater.* **2021**, Submitted.
55. Reed, R.P. Nitrogen in austenitic stainless steels. *JOM* **1989**, *41*, 16–21. [CrossRef]